Fully CMOS-compatible titanium nitride nanoantennas

Cite as: Appl. Phys. Lett. **108**, 051110 (2016); https://doi.org/10.1063/1.4941413 Submitted: 25 November 2015 . Accepted: 24 January 2016 . Published Online: 05 February 2016

Justin A. Briggs, Gururaj V. Naik, Trevor A. Petach, Brian K. Baum, David Goldhaber-Gordon, and Jennifer A. Dionne







ARTICLES YOU MAY BE INTERESTED IN

Temperature-dependent optical properties of titanium nitride Applied Physics Letters 110, 101901 (2017); https://doi.org/10.1063/1.4977840

Optical, electronic, and transport properties of nanocrystalline titanium nitride thin films Journal of Applied Physics 90, 4725 (2001); https://doi.org/10.1063/1.1403677

Electron energy loss spectroscopy of plasmon resonances in titanium nitride thin films Applied Physics Letters 108, 171107 (2016); https://doi.org/10.1063/1.4947442







Fully CMOS-compatible titanium nitride nanoantennas

Justin A. Briggs, 1,2,a) Gururaj V. Naik, Trevor A. Petach, Brian K. Baum, 2 David Goldhaber-Gordon,³ and Jennifer A. Dionne²

¹Department of Applied Physics, Stanford University, 348 Via Pueblo Mall, Stanford, California 94305, USA ²Department of Materials Science and Engineering, Stanford University, 496 Lomita Mall, Stanford, California 94305. USA

³Department of Physics, Stanford University, 382 Via Pueblo Mall, Stanford, California 94305, USA

(Received 25 November 2015; accepted 24 January 2016; published online 5 February 2016)

CMOS-compatible fabrication of plasmonic materials and devices will accelerate the development of integrated nanophotonics for information processing applications. Using low-temperature plasma-enhanced atomic layer deposition (PEALD), we develop a recipe for fully CMOScompatible titanium nitride (TiN) that is plasmonic in the visible and near infrared. Films are grown on silicon, silicon dioxide, and epitaxially on magnesium oxide substrates. By optimizing the plasma exposure per growth cycle during PEALD, carbon and oxygen contamination are reduced, lowering undesirable loss. We use electron beam lithography to pattern TiN nanopillars with varying diameters on silicon in large-area arrays. In the first reported single-particle measurements on plasmonic TiN, we demonstrate size-tunable darkfield scattering spectroscopy in the visible and near infrared regimes. The optical properties of this CMOS-compatible material, combined with its high melting temperature and mechanical durability, comprise a step towards fully CMOSintegrated nanophotonic information processing. © 2016 AIP Publishing LLC.

[http://dx.doi.org/10.1063/1.4941413]

When light interacts resonantly with nanostructured metal, the electromagnetic fields can be both highly enhanced and tightly confined. In recent years, the study of this plasmonic interaction has led to a number of exciting applications, ranging from sensing¹ and catalysis² to cancer therapeutics³ and information processing.⁴ Silver and gold have been the metals of choice for most plasmonic components. However, these materials exhibit low melting temperatures, low mechanical durability, high surface energies, and incompatibility with standard complementary metal-oxidesemiconductor (CMOS) devices. These severe limitations have inhibited full realization of many applications.⁵

To overcome these material challenges, researchers have started searching for alternative plasmonic materials.^{6–8} Many new materials have emerged, ranging from graphene⁹ and highly doped semiconductors 10 in the THz/infrared regime to aluminum¹¹ and various metal nitrides¹⁰ in the visible/near-infrared (NIR) regime.

One particularly attractive material is titanium nitride (TiN). It boasts optical properties similar to those of gold, ¹² a melting temperature of 2930 °C, 13 extreme mechanical durability, low surface energy, 14 and CMOS compatibility. TiN has already enabled high-efficiency local heating, 15 broadband absorbers in the visible 16 and IR, 17 and hyperbolic metamaterials with photonic density of states enhancement surpassing those demonstrated with silver- and gold-based devices. 18

Growth of plasmonic-quality TiN has usually relied on high-temperature sputtering. However, to maximally impact nanophotonic computing applications, a low-temperature TiN growth process that is already integrated into standard CMOS fabrication is required. Atomic layer deposition (ALD) meets this criteria, and TiN grown via low-temperature processes is already used by the semiconductor industry for metal gates¹⁹ and diffusion barriers²⁰ in CMOS devices. Because these applications require that TiN possesses sufficiently good electrical, rather than optical, properties,²¹ the dielectric function of ALD TiN is not usually sufficient to enable plasmonic applications.

In this letter, we demonstrate the first fully CMOScompatible plasmonic nanoantennas made from lowtemperature ALD TiN. Long-duration plasma-enhanced ALD (PEALD) results in TiN films that are plasmonic in the visible and NIR. Ellipsometric characterization reveals that films grown with longer plasma exposure have much better optical properties than those grown with the industrystandard recipe. X-ray photoemission spectroscopy (XPS) depth profiling indicates that this increased quality can be attributed to reduced carbon and oxygen contamination in the film. X-ray diffraction (XRD) characterization demonstrates that PEALD TiN grows epitaxially on latticematched magnesium oxide (MgO) substrates and polycrystalline on silicon substrates. The first reported optical darkfield scattering measurements of single, lithographically fabricated TiN nanopillars, corroborated by finite-difference time-domain (FDTD) simulations, demonstrate fully CMOScompatible optical nanoantennas with size-tunable plasmon resonances.

PEALD of TiN was carried out in a Cambridge Nanotech Fiji F202 system at 250 °C using a Tetrakis(dimethylamido) titanium(IV) (TDMAT) precursor²² in a nitrogen and argon environment. In the CMOS "industry standard" recipe, ²³ 20 s of plasma/cycle was used. In our "optimized" recipe, which

^{a)}Author to whom correspondence should be addressed. Electronic mail: jabriggs@stanford.edu

includes a pre-deposition chamber seasoning, a 250 °C hydrogen plasma anneal, and a post-deposition vacuum cool, the plasma time/cycle was varied from 20 to 110 s. Silicon, silicon dioxide, and MgO were used as substrates. After deposition, ellipsometric measurements were taken using a Variable Angle Spectroscopic Ellipsometer (VASE) from J.A. Woollam Co.²³

Fig. 1(a) shows the real and imaginary components of the relative permittivity of TiN on silicon, extracted from the VASE data using a Drude-Lorentz model²⁴

$$\epsilon(\omega) = \epsilon_b - \frac{\omega_p^2}{\omega^2 + i\gamma\omega} + \sum_{n=1}^3 \left(\frac{A_n \omega_n^2}{\omega_n^2 - \omega^2 - i\gamma_n \omega} \right),$$

where ω_p is the plasma frequency, ω_n and A_n are the resonance frequencies and strengths of the Lorentz oscillators, γ (γ_n) is the Drude (Lorentz) damping, and ϵ_b is the background permittivity. Two Lorentz oscillators in the UV model interband transitions while a third models losses in the NIR. Film thicknesses were determined via VASE to be between 20 nm and 90 nm depending on the number of ALD cycles (20 nm was used as the minimum thickness to avoid thin film effects).

The optical properties resulting from the standard industry recipe (the red curves in Fig. 1(a)) are poor for plasmonics applications, indicating a material that is mostly a lossy dielectric throughout the visible and NIR spectral range. However, our optimized recipe results in greatly improved optical properties, with longer plasma exposures giving a more negative $Re[\epsilon]$ and thus more metallic films.

The screened plasma frequency (ω_p^s , the frequency at which the real permittivity crosses from positive to negative) is also a useful metric for film quality because it indicates the onset of metallic behavior. A larger ω_p^s is desirable because it enables plasmonics applications at visible

wavelengths. Re[ϵ] for the industry standard TiN barely drops below zero in the entire 300 to 1700 nm spectral range, and the optimized 20 s plasma/cycle and 40 s plasma/cycle films exhibit screened plasma frequencies barely in the visible range (ω_p^s [20 s] \approx 763 nm and ω_p^s [40 s] \approx 705 nm). Longer plasma cycles, however, yield significant improvement in the optical properties. For example, the optimized 80 s plasma/cycle and 110 s plasma/cycle films have ω_p^s [110 s] \approx 622 nm.

Fig. 1(b) better explains this trend. XPS depth profiles of films grown with 20 s and 80 s of plasma per cycle, respectively, show notably different contaminant concentrations in the bulk of the films. The 20 s plasma film has $13 \pm 1\%$ oxygen and $7 \pm 1\%$ carbon, while the 80 s plasma film has $3 \pm 1\%$ oxygen and $4 \pm 1\%$ carbon. These impurities are likely causing absorption in the NIR, thus strengthening the Lorentzian contribution in the NIR and pulling $Re[\epsilon]$ towards more positive values.

We also note from the depth profile that our films are non-stoichiometric and titanium-rich. The ratio of titanium to nitrogen in the film has been shown to affect the optical properties, with excess titanium resulting in a higher plasma frequency.¹² Future studies optimizing TiN stoichiometry by varying ALD gas ratios may offer an additional means to tune the plasma frequency.

To further improve the optical properties, we annealed the films in vacuum for 2 h at several temperatures. As can be seen in Figs. 1(c) and 1(d), annealing at higher temperatures increases the screened plasma frequency and decreases $\text{Im}[\epsilon]$ at this wavelength. Anneals below 500 °C can be easily incorporated into the standard CMOS process flow, 25 but even without annealing films grown with long-duration plasma exposure exhibit screened plasma frequencies well into the visible range, enabling plasmonics applications at visible and NIR wavelengths.

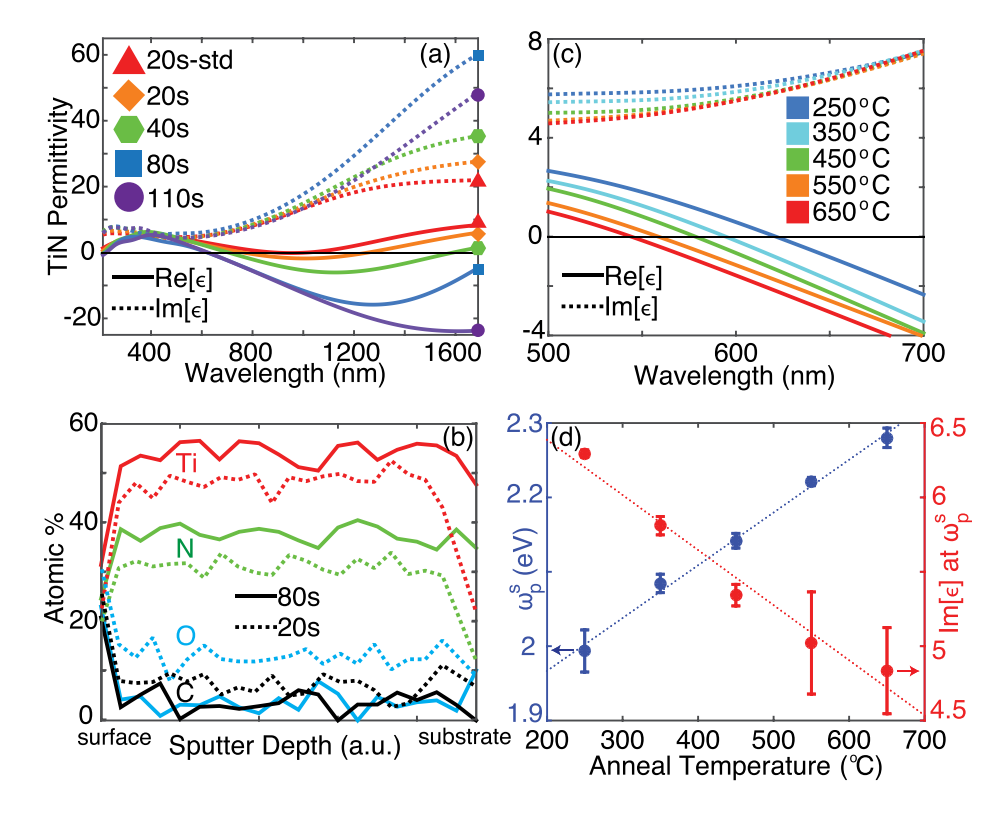


FIG. 1. Growth and characterization of CMOS-compatible TiN. (a) Relative permittivity (ϵ) of TiN grown on Si via ALD using the CMOS industry standard recipe with 20 s plasma/cycle (20 sstd) and our optimized recipe with varying plasma time; all curves not labeled as "std" are from the optimized recipe. (b) XPS depth profiles of TiN films grown on Si with 20s plasma/ cycle (dotted lines) and 80 s plasma/ cycle (solid lines) showing the concentrations of the relevant elements. (c) Relative permittivity of TiN grown with 80 s plasma per cycle and subsequently annealed in vacuum for 2h at several temperatures. (d) The screened plasma frequency (ω_n^s) and $\text{Im}[\epsilon]$ at ω_n^s for the annealed films. Error bars are one standard deviation; linear fits are provided as a guide to the eye.

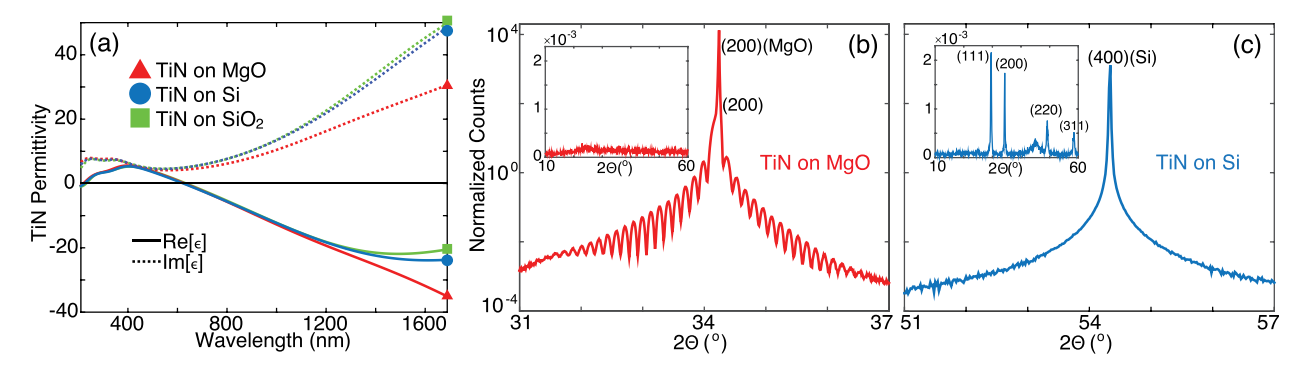


FIG. 2. Relative permittivity via ellipsometry and crystal structure via XRD of TiN films grown on Si and MgO using our optimized 110 s plasma/cycle ALD recipe. (a) Relative permittivity (ϵ) of TiN films grown on Si, SiO₂, and MgO. (b) Symmetric XRD scan around the TiN (200) peak on MgO (inset: grazing incidence scan for $\theta=0.5^{\circ}$). (c) Symmetric XRD scan around the Si (400) peak (inset: grazing incidence scan for $\theta=0.5^{\circ}$). All indexed diffraction peaks correspond to TiN except when labeled otherwise. $10\,\text{keV}$ x-rays were used for all diffraction measurements.

While silicon is the optimal substrate from the CMOS-integration perspective, MgO offers a distinct advantage as well. With lattice constants of 4.21 Å and 4.24 Å, respectively, MgO and TiN are lattice matched to within 0.71% and MgO therefore supports epitaxial growth of TiN. Fig. 2(a) shows the permittivity of TiN grown on Si, SiO₂, and MgO and demonstrates that the MgO-grown films have greater metallic character (more negative $Re[\epsilon]$) and lower loss (smaller $Im[\epsilon]$).

The improved optical properties of TiN grown on MgO versus Si can be attributed, in part, to reduced grain boundary scattering. To validate this hypothesis, we performed XRD measurements on both sets of films. As seen in Fig. 2(b), the presence of finite thickness fringes around the TiN (200) peak in the symmetric scan and the absence of any peaks in the grazing incidence scan (inset) demonstrate epitaxial growth of the TiN on MgO. On Si (Fig. 2(c)), no finite thickness fringes are observed in the symmetric scan over the 2Θ range investigated (10°–70°), and all allowed TiN peaks appear in a grazing incidence scan over the same range (inset), indicating a polycrystalline film. Scattering from the boundaries of these domains likely results in a lossier TiN on Si as compared to on MgO.

Given that ALD films are known to exhibit substrate-dependent growth, ²⁶ it is also possible that different impurity incorporation contributes to the differing optical properties. ²³ Future work focused on ALD optimization should further enhance the optical properties of TiN. Though it may compromise CMOS-compatibility, using different precursors, such as titanium tetrachloride, and exploring different deposition temperatures may lead to reduced carbon contamination. ^{27–29}

An optical nanoantenna, comprised of a single metallic nanopillar, is the basis for many plasmonic devices. To demonstrate the functionality of our CMOS-compatible TiN, we patterned our ALD films into arrays of widely spaced nanopillars and examined the scattering properties of individual nanopillars in a darkfield spectroscopy setup.

After using our optimized, 110 s plasma/cycle ALD recipe to grow 90 nm of TiN on 140 nm of thermal oxide on a Si wafer, we patterned nanopillars using electron beam lithography and reactive ion etching. We etched our sample such that each pillar consisted of a TiN cap on a SiO₂ pillar on the Si substrate. The oxide layer was included to separate the TiN

from the high-index Si which would redshift the scattering resonance of the TiN beyond the range of our detector. The inset of Fig. 3(a) shows a schematic of such a nanopillar. These structures were patterned in large-area arrays with high

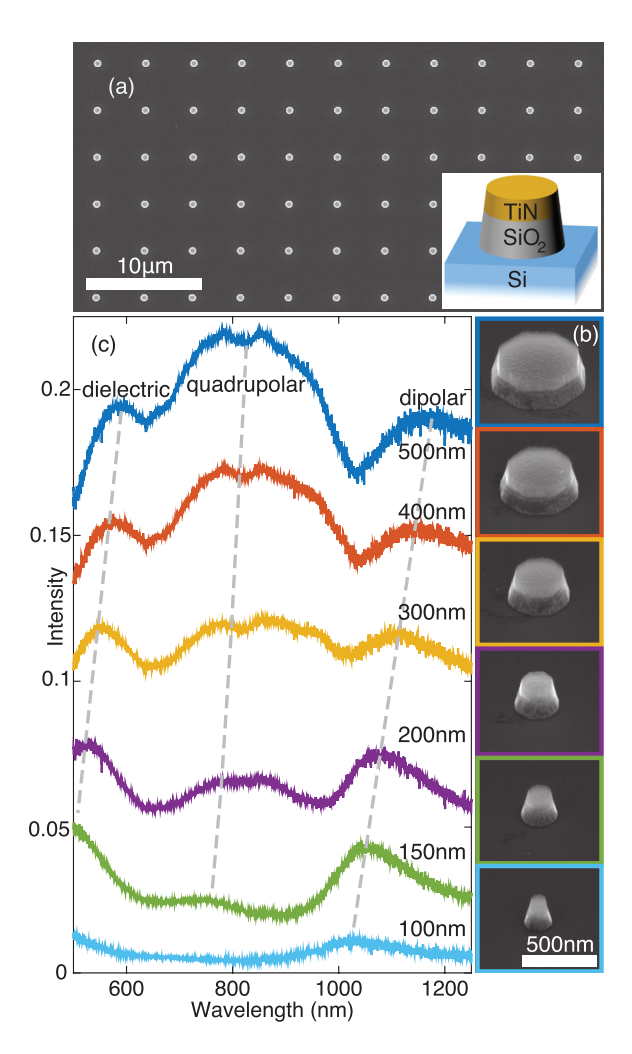


FIG. 3. Size-dependent darkfield spectroscopy of individual TiN nanostructures. (a) Wide-area SEM micrograph showing an array of TiN nanopillars (inset: schematic of a nanopillar). (b) SEM micrographs showing nanopillars of descending diameter: 500 nm, 400 nm, 300 nm, 200 nm, 150 nm, and 100 nm. (c) Darkfield scattering spectra of individual nanopillars of the same diameters shown in (b), with diameters labeled. The plasmonic dipolar, plasmonic quadrupolar, and dielectric modes are labeled, and dotted grey lines provide guides to the eye as these modes evolve with scatterer diameter.

FIG. 4. Finite-difference time-domain simulations of the nearfields of an individual 500 nm nanopillar. (a) The magnitude of the electric field in the horizontal plane through the bottom of the TiN disk, with the charge distribution overlaid, at the dipolar plasmonic resonance. (b) Same as (a), but at the quadrupolar plasmonic resonance. (c) Same as (a), but at the dielectric resonance. (d) The magnitude of the electric field in a vertical plane passing through the center of the TiN disk, at the dipolar plasmonic resonance. (e) Same as (d), but for the quadrupolar plasmonic resonance. (f) Same as (d), but for the dielectric resonance.

fidelity, as demonstrated by the scanning electron microscope (SEM) micrographs in Figs. 3(a) and 3(b).²³

After fabrication, individual nanopillars of varying diameters were examined in a darkfield microscope illuminated by a tungsten lamp and coupled to a spectrometer. Fig. 3(b) shows SEM images of single nanopillars ranging in diameter from 100 nm to 500 nm, while Fig. 3(c) shows the scattering spectra from these individual structures. Three distinct peaks evolve as the diameter of the scatterer is increased: (1) The lowest energy resonance redshifts from \sim 1020 nm to \sim 1160 nm; (2) a higher energy mode emerges around 750–900 nm; and (3) the highest energy resonance redshifts from below the detection range to just under 600 nm.

In order to understand this scattering behavior, we modeled our nanoantennas using FDTD simulations with normalincidence plane-wave illumination. The simulated scattering spectra confirm the three spectral trends present in the experiment (see supplementary material, Fig. S3),²³ though with a more pronounced redshift of the lowest energy resonance.³⁰ Field profiles and charge distributions at the simulated resonance peaks illustrate the modes that are present in our experiment. For example, Fig. 4(a) shows the magnitude of the electric field in the horizontal plane through the bottom of the 500 nm diameter TiN disk, with the charge distribution overlaid, at the lowest energy resonance. The field map and charge distribution confirm that this resonance is in fact the dipolar plasmon mode. In turn, the fields and charges at the intermediate energy mode exhibit a quadrupolar distribution, as seen in Fig. 4(b). The highest energy peak occurs above the TiN screened plasma frequency and is thus a purely dielectric resonance, as can be seen from the field maps in Figs. 4(c) and 4(f).

Figs. 4(d) and 4(e) show the plasmonic hot spots generated at the edges of the TiN disk at the dipolar and quadrupolar resonances, respectively. As illustrated by the field profile in the SiO₂ pillar in Fig. 4(e), the quadrupolar mode appears to be a hybrid plasmonic-photonic mode supported at the

interface between the TiN disk and the SiO₂ pillar. These three modes constitute a set of resonant optical responses that can be leveraged to create nanophotonic architectures operating in the entire visible/NIR regime.

We have demonstrated fully CMOS-compatible optical nanoantennas lithographically patterned from ALD TiN. Coupled with the conformal deposition capability enabled by ALD and the low surface energy of TiN, advanced plasmonic information processing architectures could be easily integrated into existing CMOS device platforms. Further, the superior mechanical and thermal durability of TiN will allow devices that operate in extreme conditions and with long lifetimes, including thermal photovoltaic emitters and heat-assisted magnetic recording heads. And not least, this can now be achieved using industry-standard materials and processes, thus expanding the scope of plasmonics to include even more diverse applications in the future.

Support from an AFOSR PECASE grant (FA9550-15-1-0006) and Northrop Grumman are gratefully acknowledged. J.A.B. was supported by a NSF GRF (2012122469). G.V.N. was supported by a DOE EFRC (DE-SC0001293). T.A.P. was supported under a SGF. Part of this work was performed at the Stanford's SNF and SNSF, and was supported by DOE, LDRD funding (DE-AC02-76SF00515). Use of the SSRL, SLAC Natl. Accelerator Lab, is supported by the U.S. DOE (DE-AC02-76SF00515).

¹J. N. Anker, W. P. Hall, O. Lyandres, N. C. Shah, and J. Zhao, Nat. Mater. 7, 442–453 (2008).

²P. Christopher, H. Xin, A. Marimuthu, and S. Linic, Nat. Mater. 11, 1044–1050 (2012).

³D. P. O'Neal, L. R. Hirsch, N. J. Halas, J. D. Payne, and J. L. West, Cancer Lett. **209**, 171–176 (2004).

⁴W. A. Challener, C. Peng, A. V. Itagi, D. Karns, W. Peng, Y. Peng, X. Yang, X. Zhu, N. J. Gokemeijer, Y. T. Hsia *et al.*, Nat. Photonics 3, 220–224 (2009).

⁵P. R. West, S. Ishii, G. V. Naik, N. K. Emani, V. M. Shalaev, and A. Boltasseva, Laser Photonics Rev. 4, 795–808 (2010).

⁶G. V. Naik, V. M. Shalaev, and A. Boltasseva, Adv. Mater. **25**, 3264–3294 (2013)

⁷A. Boltasseva and H. A. Atwater, Science **331**, 290–291 (2011).

⁸M. G. Blaber, M. D. Arnold, and M. J. Ford, J. Phys.: Condens. Matter 22, 143201 (2010)

⁹L. Ju, B. Geng, J. Horng, C. Girit, M. Martin, Z. Hao, H. A. Bechtel, X. Liang, A. Zettl, Y. R. Shen, and F. Wang, Nat. Nanotechnol. 6, 630–634 (2011).

¹⁰G. V. Naik, J. Kim, and A. Boltasseva, Opt. Mater. Express 1, 1090–1099 (2011).

¹¹M. W. Knight, N. S. King, L. Liu, H. O. Everitt, P. Nordlander, and N. J. Halas, ACS Nano 8, 834–840 (2014).

¹²G. V. Naik, J. L. Schroeder, X. Ni, A. V. Kildishev, T. D. Sands, and A. Boltasseva, Opt. Mater. Express 2, 478–489 (2012).

U. Guler, A. Boltasseva, and V. M. Shalaev, Science 344, 263–264 (2014).
C.-C. Sun, S.-C. Lee, W.-C. Hwang, J.-S. Hwang, I.-T. Tang, and Y.-S. Fu, Mater. Trans. 47, 2533–2539 (2006).

¹⁵U. Guler, J. C. Ndukaife, G. V. Naik, A. G. A. Nnanna, A. V. Kildishev, V. M. Shalaev, and A. Boltasseva, Nano Lett. 13, 6078–6083 (2013).

¹⁶W. Li, U. Guler, N. Kinsey, G. V. Naik, A. Boltasseva, J. Guan, V. M. Shalaev, and A. V. Kildishev, Adv. Mater. 26, 7959–7965 (2014).

¹⁷S. Bagheri, C. M. Zgrabik, T. Gissibl, A. Tittl, F. Sterl, R. Walter, S. De Zuani, A. Berrier, T. Stauden, G. Richter *et al.*, Opt. Mater. Express 5, 2625–2633 (2015).

¹⁸G. V. Naik, B. Saha, J. Liu, S. M. Saber, E. A. Stach, J. M. K. Irudayaraj, T. D. Sands, V. M. Shalaev, and A. Boltasseva, Proc. Natl. Acad. Sci. U. S. A. 111, 7546–7551 (2014).

¹⁹K. Mistry, C. Allen, C. Auth, B. Beattie, D. Bergstrom, M. Bost, M. Brazier, M. Buehler, A. Cappellani, R. Chau *et al.*, Tech. Dig. - Int. Electron Devices Meet. **2007**, 247.

- ostito-s bliggs et
- ²⁰S. Venkatesan, A. V. Gelatos, S. Misra, B. Smith, R. Islam, J. Cope, B. Wilson, D. Tuttle, R. Cardwell, S. Anderson *et al.*, Tech. Dig. Int. Electron Devices Meet. **1997**, 769.
- ²¹J. Musschoot, Q. Xie, D. Deduytsche, S. Van den Berghe, R. L. Van Meirhaeghe, and C. Detavernier, Microelectron. Eng. 86, 72–77 (2009).
- ²²F. Fillot, T. Morel, S. Minoret, I. Matko, S. Maîtrejean, B. Guillaumot, B. Chenevier, and T. Billon, Microelectron. Eng. 82, 248–253 (2005).
- ²³See supplementary material at http://dx.doi.org/10.1063/1.4941413 for details on ALD, ellipsometry, XPS, XRD, DC electrical characterization, nanofabrication, darkfield spectroscopy, and numerical simulations.
- ²⁴M. Dressel and G. Grüner, "Electrodynamics of Solids: Optical Properties of Electrons in Matter" (Cambridge University Press, 2002).
- ²⁵J. D. Plummer, M. D. Deal, and P. B. Griffin, *Silicon VLSI Technology: Fundamentals, Practice and Modeling*, Prentice Hall Electronics and VLSI Series (Prentice Hall, 2000).
- ²⁶S. W. Lee, B. J. Choi, T. Eom, J. H. Han, S. K. Kim, S. J. Song, W. Lee, and C. S. Hwang, Coord. Chem. Rev. 257, 3154–3176 (2013).
- ²⁷H. Van Bui, A. W. Groenland, A. A. I. Aarnink, R. A. M. Wolters, J. Schmitz, and A. Y. Kovalgin, J. Electrochem. Soc. 158, H214 (2011).
- ²⁸E. Langereis, S. B. S. Heil, M. C. M. van de Sanden, and W. M. M. Kessels, J. Appl. Phys. **100**, 023534 (2006).
- ²⁹H. Kim, J. Vac. Sci. Technol. B **21**, 2231 (2003).
- ³⁰L. Jiang, T. Yin, Z. Dong, M. Liao, S. J. Tan, X. M. Goh, D. Allioux, H. Hu, X. Li, J. K. W. Yang, and Z. Shen, ACS Nano 9, 10039–10046 (2015).